



HAL
open science

Insight on precipitate evolution during additive manufacturing of stainless steels via in-situ heating-cooling experiments in a transmission electron microscope

Meriem Ben Haj Slama, Lluís Yedra, Eva Heripre, Manas V Upadhyay

► To cite this version:

Meriem Ben Haj Slama, Lluís Yedra, Eva Heripre, Manas V Upadhyay. Insight on precipitate evolution during additive manufacturing of stainless steels via in-situ heating-cooling experiments in a transmission electron microscope. *Materialia*, inPress, 10.1016/j.mtla.2022.101368 . hal-03570116

HAL Id: hal-03570116

<https://polytechnique.hal.science/hal-03570116v1>

Submitted on 13 Feb 2022

HAL is a multi-disciplinary open access archive for the deposit and dissemination of scientific research documents, whether they are published or not. The documents may come from teaching and research institutions in France or abroad, or from public or private research centers.

L'archive ouverte pluridisciplinaire **HAL**, est destinée au dépôt et à la diffusion de documents scientifiques de niveau recherche, publiés ou non, émanant des établissements d'enseignement et de recherche français ou étrangers, des laboratoires publics ou privés.

Insight on precipitate evolution during additive manufacturing of stainless steels via in-situ heating-cooling experiments in a transmission electron microscope

Meriem Ben Haj Slama^{a,b,1}, Lluís Yedra^{b,c,2}, Eva Heripre^b, Manas V. Upadhyay^{a,*}

^a Laboratoire de Mécanique des Solides (LMS), CNRS UMR 7649, Ecole Polytechnique, Institut Polytechnique de Paris, 91128 Palaiseau, France

^b Laboratoire de Mécanique des Sols, Structures et Matériaux (MSSMat), CNRS UMR 8579, CentraleSupélec, Université Paris-Saclay, 91190 Gif-sur-Yvette, France

^c Laboratoire Structures, Propriétés et Modélisation des Solides (SPMS), CNRS UMR 8580, CentraleSupélec, Université Paris Saclay, 91190 Gif-sur-Yvette, France

* Corresponding author, email: manas.upadhyay@polytechnique.edu

Abstract

During additive manufacturing of alloys, just after local heat-matter interactions, a molten material undergoes rapid solidification. Then, for the rest of the building time, it is subjected to cooling/heating cycles in the solid-state i.e., solid-state thermal cycling. The thermo-mechanical forces generated during solid-state thermal cycling can trigger a plethora of micro-mechanisms that can bring about significant microstructural changes that determine the eventual mechanical properties of as-built parts. In this work, the aim is to gain insight on solid-state thermal cycling-driven evolution of submicron-sized precipitates in an austenitic stainless steel using transmission electron microscopy. To that end, thin-film lamellae are extracted from a pre-built sample and subjected to different *in-situ* solid-state thermal cycles inside a transmission electron microscope. The solid-state thermal cycles are designed to understand the role of temperature amplitude and rates, number and type of thermal cycles, and post-process annealing on precipitate evolution. High angle annular dark field imaging and energy dispersive X-ray spectroscopy before and after each thermal cycle provide a deep insight on the contribution of different thermal cycling factors on the evolution of precipitate composition, size and morphology. Common trends include diffusion of Mn and Si from Mn-Si-rich oxides into the surrounding matrix, formation of Cr rings around oxide precipitates and S redistribution in non-oxide precipitates. Similar Cr rings and S distributions were also found in precipitates in as-built samples studied in (Upadhyay et al., Sci. Rep. 11 (2021) 10393), which strongly supports the representativeness of these results with respect to what occurs during additive manufacturing.

Keywords: *In situ*, transmission electron microscopy (TEM), stainless steel, precipitate, additive manufacturing

1. Introduction

During additive manufacturing (AM) of alloys, just after local heat-matter interactions, the material rapidly solidifies. Then, for the rest of the AM process, it is subjected to cooling-heating cycles in the solid-state i.e., solid-state thermal cycling (SSTC), also known as intrinsic heat treatment, at varying temperature amplitudes and rates. Current experiment [1–11] and modeling [12–17] efforts are overwhelmingly focused on understanding microstructure formation due to

¹ Current address: CESI École d'Ingénieurs, 54500 Vandœuvre-lès-Nancy, France

² Current address: University of Barcelona, Department of Electronics and Biomedical Engineering and Institute of Nanoscience and Nanotechnology (IN2UB), 08028 Barcelona, Catalonia, Spain

melt-pool dynamics and rapid solidification. While these phenomena are important to understand microstructure genesis during AM, however, they are insufficient to understand the formation of the final microstructure of as-built parts. A comprehensive understanding of the microstructure obtained at the end of the AM process requires studying the role of SSTC.

During initial stages of SSTC, the heated solid material is subjected to high temperature amplitudes (close to the melting point) and high cooling/heating rates ($10^2 - 10^5$ K/s during laser metal deposition (LMD) [18] – a directed energy deposition (DED) approach, and $10^6 - 10^7$ K/s during selective laser melting (SLM) – a powder bed fusion (PBF) approach [19]). During later stages of SSTC, a nearly steady-state heat transfer occurs, typically at temperatures higher than the room temperature. The thermo-mechanical driving forces during SSTC could trigger a plethora of micro-mechanisms such as precipitation, micro-segregation, dislocation dynamics and defect interactions, solid-state phase transformations, recrystallization, grain growth, etc. These micro-mechanisms could result in an evolution of the microstructure and internal stresses. Consequently, the (final) as-built microstructure can be significantly different from the as-solidified microstructure. Furthermore, some as-built samples are also subjected to post-process annealing, which is a solid-state heat treatment that can significantly affect the existing precipitate structure in as-built samples.

A handful of scanning electron microscopy (SEM) and transmission electron microscopy (TEM) studies on as-built alloys [20–22] have reported microstructural phenomena whose presence is difficult to explain from a solidification standpoint; it has been suggested that these phenomena result from SSTC-based micro-mechanisms. Meanwhile, a recent ex-situ synchrotron X-ray and neutron diffraction study [23] has revealed strong residual stress gradients along building and printing directions, which should result from defect structures formed during SSTC. However, relying solely on post-build analyses is insufficient to separate the role of SSTC from that of solidification on the microstructure formation. Univocally separating their roles requires performing a one-to-one comparison of microstructure states before and after SSTC.

The main aim of this work is to perform such a one-to-one comparison in order to understand the role of different factors of SSTC such as temperature amplitude and rates, the number and type of SSTC, as well as post-process annealing on the evolution of precipitates occurring in an as-built 316L-type austenitic stainless steel (316LSS) manufactured via LMD.

Amongst the several features present in the hierarchical AM microstructure of 316LSS fabricated either via LMD or SLM (henceforth called LMD 316LSS or SLM 316LSS), submicron-sized precipitates play an important role in determining the material response [24,25]. It is therefore crucial to understand their possible evolution due to SSTC during AM or during annealing of as-built samples. Until recently, precipitates occurring in as-built LMD 316LSS or SLM 316LSS were reported to be only Mn-Si-rich oxide precipitates [22,24–29]. However, in a recent TEM study on five lamellae extracted from an LMD 316LSS thin-wall, Upadhyay et al. [30] reported the presence of a large volume fraction of non-oxide precipitates including sulfides, carbides, phosphides and intermetallics, along with Mn-Si-rich oxide precipitates. The non-oxide precipitates were found to be smaller in their average size in comparison to the oxide precipitates. An investigation into the origin of these non-oxide precipitates [30], with the help of finite element and precipitation kinetics simulations, revealed that non-oxide precipitates can indeed occur in LMD 316LSS but not in SLM 316LSS. The simulation results also suggested that precipitates could form/disappear and evolve in the solid-state.

In this work, we propose to perform in-situ TEM SSTC experiments in order to gain insight on the role of different factors of SSTC on the evolution of precipitates during LMD of 316LSS. There are several advantages to performing in-situ SSTC inside a transmission electron

microscope: (i) since AM is not performed, there is no need to use feedstock material, which alleviates equipment contamination/damage concerns, (ii) transmission electron microscopes typically operate under high vacuum or inert gas environments, which significantly reduces the risk of oxidation of the sample, (iii) it is possible to dissect the temperature vs time curve and study the role of different stages of SSTC on microstructure evolution, (iv) it is possible to follow the evolution of submicron-sized defects such as precipitates at very high spatial resolution.

While TEM is well suited to obtain information with atomic-level resolution, however, most transmission electron microscopes cannot obtain high temporal resolution (with the notable exception of dynamic-TEM [31,32]), which makes it difficult to perform *operando* measurements during AM. Furthermore, performing AM inside any electron microscope is not advisable because the violent heat-matter interactions that occur during any AM process can severely damage the microscope. In order to overcome these shortcomings, we adopt an *in-situ* stop-and-start approach. The key idea is to first build 316LSS samples via LMD and extract TEM lamellae from these samples. Next, pre-characterize these lamellae inside a transmission electron microscope. Then, while they are still inside the microscope, subject them to additional SSTC that they would have experienced, if the AM process had continued.

The remainder of the article is divided in the following manner. The 316LSS feedstock composition and fabrication process, the experimental setup to perform in-situ SSTC inside a transmission electron microscope, and the TEM analysis techniques are recalled in section 2. The results of the different in-situ TEM SSTC experiments are presented in section 3 followed by a discussion in section 4. The discussion section focuses on identifying the general trends occurring for all SSTCs and understanding their possible origin, and then on understanding the role of temperature amplitude, temperature rates, the number and type of SSTCs, and post-process annealing on precipitate evolution. The conclusions of this study are presented in section 5. A supplementary document is provided with some statistical data and images to support the results and discussions.

2. Material and experimental setup

The material and most of the experimental setup used in this work has been described in detail in Upadhyay et al. [30]. In the following, only the essential details are recalled for the sake of completeness and self-sufficiency of this paper.

A 316LSS powder with particle size range 45 μm – 90 μm is used as feedstock. It was produced via inert gas atomization [33]. The wrought alloy used to manufacture this powder had the chemical composition in weight percent (wt. %): Fe – balance, Cr – 16.9, Ni – 12.7, Mo – 2.5, Mn – 1.5, Si – 0.7, P – 0.015, C – 0.011 and S – 0.005. According to [33], presence of trace amounts of oxygen in the atomization chamber may introduce up to 0.05 wt. % of O into the 316LSS powder during the process. More details on the powder can be found in [30] and the references therein.

Using an LMD machine, the 316LSS powder was used to print a single-track 3-layer wall on a hot-rolled 316LSS substrate via a bidirectional (forth-back-forth) scanning strategy (Fig. 1a). The main idea behind printing a 3-layer wall is to extract TEM lamellae that can be subjected to additional SSTC of different types and number of cycles in order to reproduce the SSTC that the material would have seen if one were to build, for example, a tall thin-wall/shell-type structure, or a short thin-wall with a few layers, which is typically done to repair broken parts. The LMD parameters used to print this wall are: (i) Laser power – 225 W, (ii) scan speed – 2000 mm/min, (iii) powder flow rate – 6.5 g/min, (iv) initial vertical position of focusing head above sample – 3.5 mm, and (v) vertical displacement of focusing head – 0.2 mm after deposition of each layer. The

as-built wall has dimensions 100 mm x 0.8 mm x 0.6 mm. More details on the LMD of this wall can be found in [30].

The as-built wall and substrate were mechanically cut near the mid-section and along the direction normal to the build and print directions (sections A-A, B-B and C-C in Fig. 1b, c and d, respectively). The cross-sections were then polished and analyzed via SEM using a FEI Quanta 650 FEG Environmental-SEM microscope equipped with the Symmetry® detector (Oxford Instruments) for Electron Back-Scattered Diffraction (EBSD) measurements; more details on the polishing strategy and acquisition of EBSD maps can be found in [30].

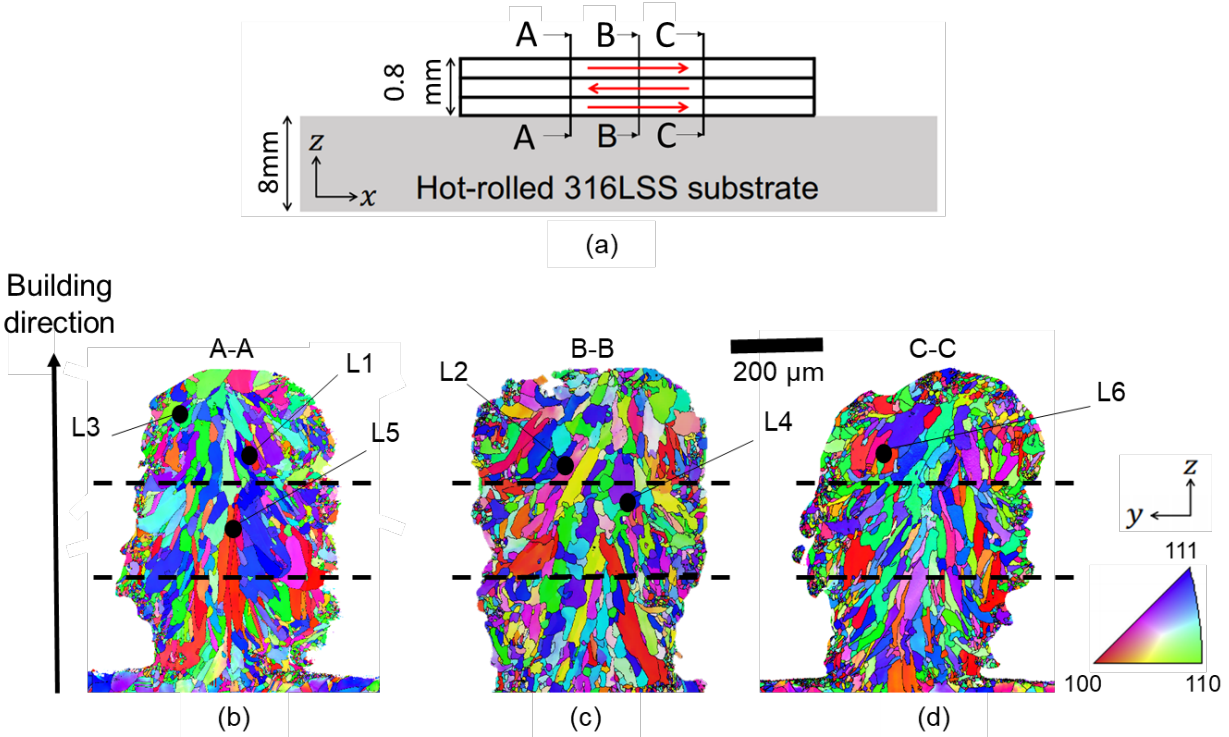


Figure 1: Illustration showing the design strategy and EBSD maps of the LMD 316LSS as-built wall from which TEM lamellae have been extracted (a) A not-to-scale illustration adapted from [30] (obtained through Creative Commons Attribution 4.0 International [CC by 4.0](https://creativecommons.org/licenses/by/4.0/) license) of the LMD 316LSS as-built wall on a hot-rolled 316LSS substrate; red arrows show the printing direction of each layer. Sections A-A (same as in [30] (obtained through Creative Commons Attribution 4.0 International [CC by 4.0](https://creativecommons.org/licenses/by/4.0/) license)), B-B and C-C correspond to the cross-sections where EBSD mapping (b), (c) and (d) was performed. Color coding of the EBSD maps is according to the IPF along the building direction.

Next, the polished sample was transported to a FEI Helios Nanolab 660 dualbeam SEM microscope equipped with a dual beam Focused Ion Beam (FIB). The FIB-SEM is used to extract 6 thin-film (~100 nm in thickness) TEM lamellae, L1 – L6, from the three cross-sections shown in Fig. 1 using the standard lift-out process. Lamellae L1, L2, L3 and L6 were taken from the topmost layer of the 3-layer wall. Therefore, the material of these lamellae had been subjected to rapid solidification followed by rapid cooling in the solid-state. Lamellae L4 and L5 were taken from the middle layer and they had experienced a solidification-cooling-heating-cooling cycle.

Each lamella was attached onto an electrothermal chip, which can be inserted into an electrothermal TEM holder (Fusion Select Protochips®). This holder is designed to be used in a high-resolution aberration-corrected FEI Titan³ G2 TEM. Using this holder, it is possible to subject

the TEM lamellae to heating-cooling cycles up to 1473 K (1200 °C) at temperature rates of 10^6 K/s (high rates that can be encountered during AM).

The Titan³ G2 TEM microscope has the capability to perform High Angle Annular Dark Field (HAADF) imaging in STEM (Scanning-TEM) mode, which is useful to identify locations of chemical heterogeneities. It also has the capability to perform Energy Dispersive X-ray Spectroscopy (EDS) in order to characterize the chemical composition of the lamellae. These capabilities were used to study precipitates in all the lamellae. The EDS maps were performed with an acquisition time of 10 min with operating conditions of 20000 counts per second and 300 keV. EDS spectra were deconvoluted and quantified as described in [30]. The quantified EDS spectra were also used to generate EDS line profile plots in order to study the composition variation within each precipitate in all lamellae.

Finally, precipitate sizes were determined from TEM images using the ImageJ software. The size measure used for comparison is the “equivalent diameter”, which is the diameter of a circle that has the same area as the area of a precipitate.

In what follows, the HAADF images and EDS chemical maps of the extracted lamellae L1, L3 and L5 and their precipitates in their initial state are the same as the lamellae L1, L3 and L2, respectively, and their precipitates in Upadhyay et al. [30] (obtained through Creative Commons Attribution 4.0 International [CC by 4.0](https://creativecommons.org/licenses/by/4.0/) license). These images and maps are shown in the present work to make it possible to perform a one-to-one comparison between the before and after SSTC states of these lamellae.

3. Results

Figure 2 shows the HAADF STEM images and EDS chemical maps of lamellae L1 – L6 in their initial state i.e., prior to any additional SSTC inside TEM. For the six lamellae, cellular solidification structures with low concentration of Fe and high concentration of Cr and Mo can be observed in the EDS maps. In addition, for L1, L4 and L5, a higher concentration of Mn can also be observed at the location of the Cr and Mo microsegregations. The long-axes of these structures are aligned with the crystal growth direction during solidification; a phenomenon that is widely accepted [25,34,35]. In L1, the long-axis is aligned with the horizontal direction because the lamella was extracted in a direction nearly parallel to the growth direction of the grain to which it had belonged [30]. In L2, L4, L5 and L6, the cellular structures have a grid-like cross-section because the lamellae have been extracted in a direction normal to the growth direction of their respective grains. In L3, it is difficult to discern the cellular structures because the lamella was extracted in a direction forming an angle $< 90^\circ$ with the growth direction of its grain [30]. Nevertheless, a Y-shaped band can be observed in its Fe, Cr and Mo maps [30].

47 precipitates have been identified in these lamellae: 16 in L1, 5 in L2, 2 in L3, 8 in L4, 5 in L5 and 11 in L6. In order to facilitate identifying the precipitates and differentiating between them, the classification scheme and the nomenclature proposed in [30] is used (Table 1). Based on this classification scheme, 24 precipitates (51%) are oxides, 2 precipitates (4%) are non-oxides and 15 precipitates (45%) are mixed. A majority of precipitates are located near or within the microsegregation walls.

Next, the lamellae were subjected to different SSTC inside the TEM in order to study the effect of the temperature amplitude, temperature rate, the number and type of SSTC, and the effect of annealing. The increase/decrease in elemental compositions of each precipitate after every SSTC is reported in supplementary data table S1.

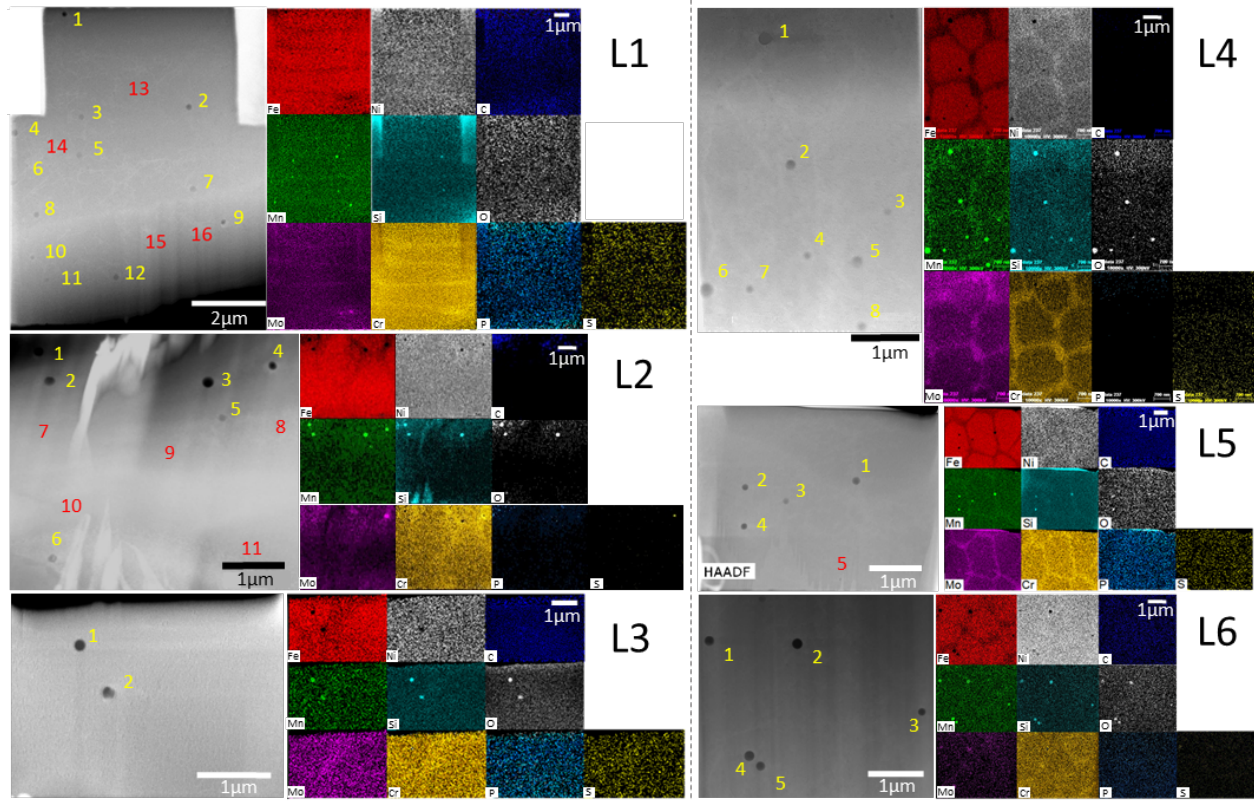


Figure 2: HAADF STEM images and EDS chemical maps of lamellae L1-L6. Images for lamellae L1, L3 and L5 are the same as lamellae L1, L3 and L2, respectively, in [30] (obtained through Creative Commons Attribution 4.0 International [CC by 4.0](https://creativecommons.org/licenses/by/4.0/) license). Similar to [30], easily visible precipitates in the HAADF images are numbered in yellow font and those detected after high-resolution imaging are numbered in red font. EDS map scale of each lamella are shown in their C map.

Table 1: Classification and nomenclature of precipitates in lamellae L1 – L6 adopted from [30]. Precipitates are classified into oxides, non-oxides and mixed based on the oxygen content and brightness in the HAADF image with respect to the surrounding matrix; the definitions are kept the same as presented in [30] (obtained through Creative Commons Attribution 4.0 International [CC by 4.0](https://creativecommons.org/licenses/by/4.0/) license). Each precipitate is numbered according to the sequence shown in the corresponding HAADF image in Fig. 2 and the number of the lamella to which it belongs is added as a subscript.

Precipitate	Description	Nomenclature					
		L1 [30]	L2	L3 [30]	L4	L5 [30]	L6
Oxide	Single inclusion with nearly uniform composition, typically Mn-Si-rich. Contains higher O than the matrix and appears darker than matrix in the HAADF image [30]	P2 ₁ -P8 ₁ , P10 ₁ , P11 ₁	P1 ₂ , P2 ₂ , P11 ₂	P1 ₃	P3 ₄ , P4 ₄ , P6 ₄ -P8 ₄	P3 ₅	P1 ₆ , P2 ₆ , P6 ₆ P4 ₆ , P5 ₆
Non-oxide	Single inclusion with nearly uniform composition. Contains lesser oxygen than the matrix and appears brighter than oxide precipitates in HAADF images [30]	P16 ₁	P5 ₂	-	-	-	-

Mixed	Two or more inclusions with different chemical compositions [30]	P1 ₁ , P9 ₁ , P12 ₁ - P15 ₁	P3 ₂ , P4 ₂ , P6 ₂ - P10 ₂	P2 ₃	P1 ₄ , P2 ₄ , P5 ₄	P1 ₅ , P2 ₅ , P4 ₅ , P5 ₅	-
-------	--	--	---	-----------------	---	--	---

3.1 Role of temperature amplitude

In order to study the effect of the temperature amplitude, L1 was subjected to the following two single heating-cooling cycles starting and ending at the Room Temperature (RT). The magnitude of the heating and cooling rates for both cycles are 4000 K/s. L1 was first subjected to SSTC1a (Fig. 3a), which involves heating from RT to 500 °C and cooling down to RT. It was then subjected to SSTC1b (Fig. 3b), which involves heating from RT to 1000 °C and cooling down to RT. HAADF and EDS characterization were performed after each SSTC. Fig. 3c shows the HAADF images and EDS chemical maps of some elements for 5 oxides, 1 non-oxide and 2 mixed precipitates in L1 in the initial, after SSTC1a and after SSTC1b states. The size evolution of all precipitates is plotted in Fig. 4.

3.1.1 Initial state

The initial state of L1 has been described in detail in [30]. It contained 16 precipitates: 9 oxides (P2₁ – P8₁, P10₁ and P11₁), 1 non-oxide rich in Mo-Cr-P-S (P16₁) and 6 mixed precipitates (P1₁, P9₁ and P12₁ – P15₁). Mixed precipitates present different complex combinations of oxide and non-oxide zones/inclusions. P1₁ is a combination of 5 small oxide inclusions and 3 zones: (i) an Mn-Si-rich oxide zone (ii) a Cr-Mo-P-S-rich non-oxide zone that partially overlaps the oxide zone, and (iii) a non-oxide Cr-Mo-P-S-rich zone. P9₁ also has three zones: (i) an Mn-Si-rich oxide zone (ii) a superposition of the oxide and the surrounding matrix, and (iii) a Cr-Mo-P-S-rich non-oxide inclusion. P12₁ has a large Mn-Si-rich oxide inclusion and a small Cr-Mo-rich non-oxide inclusion. P13₁, P14₁ and P15₁ have a central Mn-Mo-S inclusion surrounded respectively by Cr-rich, Cr-P-rich and Cr-Mo-P-rich inclusions.

3.1.2 After SSTC1a

SSTC1a did not result in any change in the oxides. However, it induced some changes to the elemental concentrations in some non-oxide and mixed precipitates; this was deduced from the changes (increase/decrease) in maximum concentration values reported in the supplementary data Table S1. In particular, notable redistributions in the S and Mo concentrations occurred in P1₁ and P9₁. With respect to precipitate sizes, in general, SSTC1a does not result in a significant change; an exception is the significant reduction in the size of zone 3 in P1₁.

3.1.3 After SSTC1b

Focusing first on the oxides, SSTC1b resulted in a partial or total diffusion of Mn from P3₁ – P8₁ and P11₁ into the surrounding matrix. In some cases (P3₁, P5₁, P6₁, P8₁ and P11₁), morphological changes were observed as can be seen in the HAADF images in Fig. 3; initial elliptic shapes evolved into irregular concave shapes. Furthermore, different shapes and amounts of micro-segregations of Cr appeared either in or around P3₁, P4₁, P6₁, P8₁ and P11₁. For example, Cr redistributed in P3₁ to form a segregation band inside the precipitate and a ring around it. Amongst all the oxides, only P2₁ and P10₁ did not show any change.

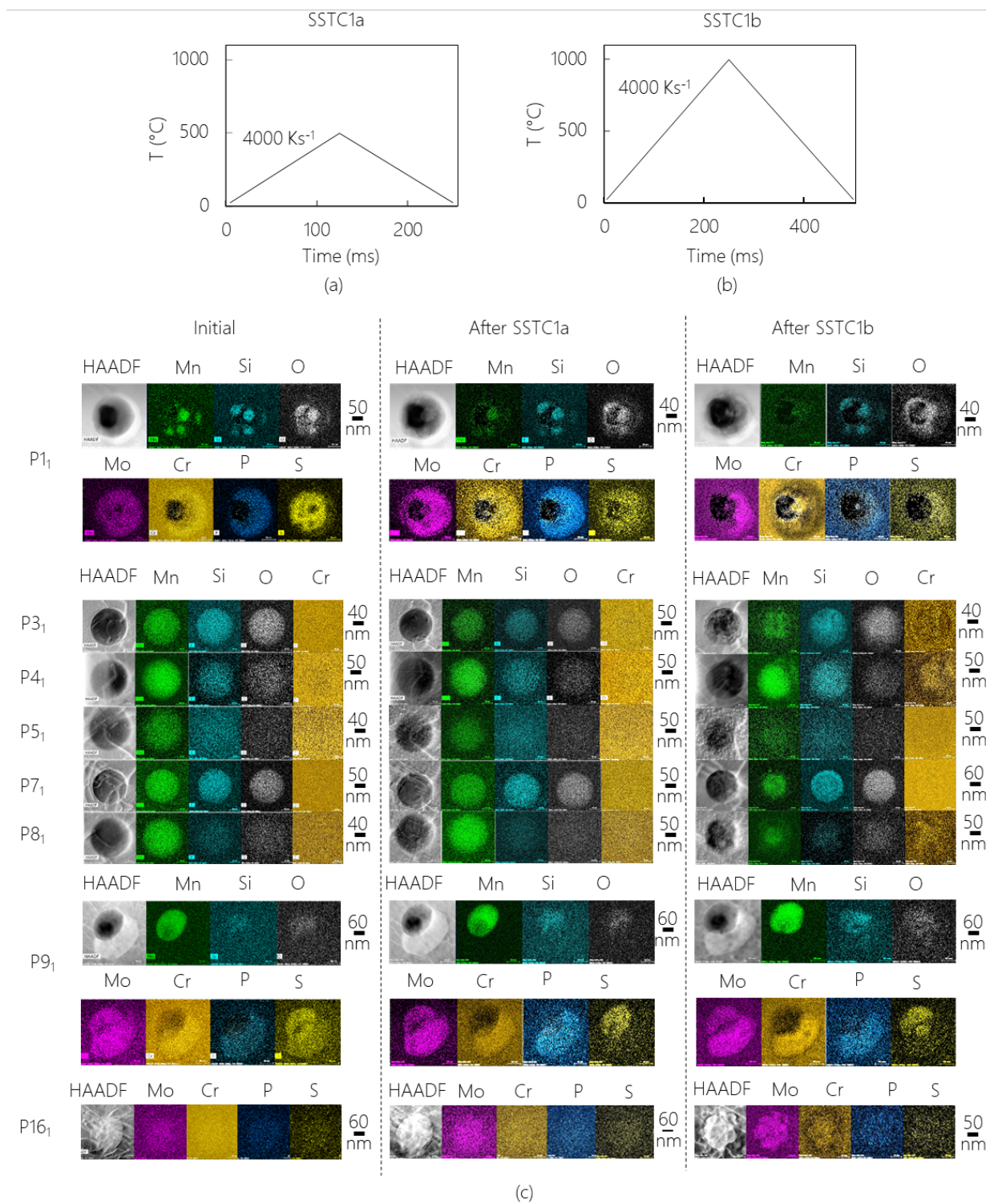


Figure 3: The temperature v/s time curves of (a) SSTC1a and (b) SSTC1b and the (c) HAADF STEM images and EDS maps of some precipitates before SSTC (same as in [30] obtained through Creative Commons Attribution 4.0 International [CC by 4.0 license](https://creativecommons.org/licenses/by/4.0/)), and after SSTC1a and SSTC1b.

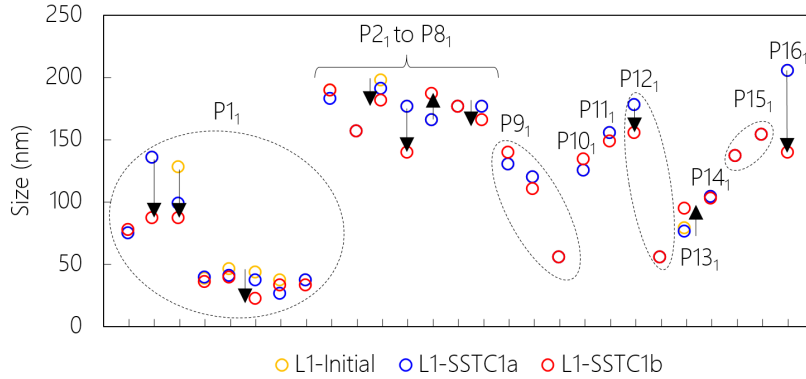


Figure 4: Evolution of precipitates and their associated zones/ inclusions for L1 before and after both SSTCs. Inclusions belonging to the same mixed precipitates are inside dashed ellipses. Arrows indicate a significant increase/decrease.

For the non-oxide precipitate $P16_1$, a significant morphological change from the initial (and after SSTC1) elliptic shape to an irregular concave shape was observed. It was accompanied by a depletion in Cr along the precipitate boundary.

Similar to the oxide precipitates, the oxide inclusions in mixed precipitates also experienced the diffusion of Mn into the surrounding matrix. For $P13_1$ and $P14_1$, the concentration of Cr and Cr-P increased in their respective rings. Meanwhile, for $P1_1$ and $P9_1$, additional redistribution and decrease occurred in the S-content together with a depletion in Cr on the precipitate surfaces.

In general, the changes in size are much larger after SSTC1b than after SSTC1a. The size of 13 precipitates/inclusions decreased significantly whereas the size of only 4 precipitates/inclusions increased. The biggest reduction in size occurred for the non-oxide precipitate $P16_1$ after SSTC1b.

3.2 Role of temperature rate

In order to study the effect of different temperature rates on precipitate evolution, lamellae L2 and L3 were heated from RT to the same temperature amplitude of 800 °C and cooled down back to RT but at different heating/cooling rates. The heating/cooling rate used for L2 and L3 were 4000 K/s (SSTC2) and 1000 K/s (SSTC3), respectively. Fig. 5 shows the temperature v/s time curve of SSTC2 and the HAADF images and EDS chemical maps for 2 oxides and 2 mixed precipitates in L2. Fig. 6 shows the temperature v/s time curve of SSTC3 and the HAADF images and EDS chemical maps of the two precipitates in L3. Fig. 7a and 7b show the size evolution of all the precipitates in L2 and L3, respectively.

3.2.1 Initial states

In the initial state, L2 contained 11 precipitates: 3 oxides ($P1_2$, $P7_2$ and $P11_2$), 1 non-oxide ($P5_2$) and 7 mixed ($P2_2$, $P3_2$, $P4_2$, $P6_2$, $P8_2$, $P9_2$ and $P10_2$). $P5_2$ is an Mn-Mo-S-rich non-oxide precipitate. $P3_2$ is a superposition of a large Mn-Si-rich oxide inclusion and 2 small oxide inclusions that are richer in Si and meager in Mn in comparison to the larger oxide inclusion. $P4_2$ has 3 small Mn-Si-rich oxide inclusions and 2 large non-oxide inclusions: (i) an Mn-S-rich inclusion that is surrounded by (ii) a crescent-shaped Cr-Mo-P-rich inclusion. $P6_2$ has an Mn-Mo-S-rich inclusion growing on an Mn-Si-rich oxide inclusion. $P8_2$ is an Mn-S-rich inclusion surrounded by a crescent-shaped Mo-Cr-P-rich zone. $P2_2$, $P9_2$ and $P10_2$ are oxide inclusions surrounded by Cr-rich rings.

In the initial state, L3 contained only 2 precipitates, P1₃ and P2₃. P1₃ is an Mn-Si-rich oxide. P2₃ is a mixed precipitate composed of 5 inclusions: 1 central Mn-Si-oxide inclusion and 2 pairs of non-oxide inclusions (Mn-S-Mo-rich and Mo-Cr-P-rich).

3.2.2 L2 after SSTC2

Similar to the case of SSTC1b on L1, SSTC2 on L2 resulted in the diffusion of Mn from the oxide precipitates to the matrix and the formation of a Cr ring around one of the oxides. The Mn-S-Mo-rich non-oxide P5₂ dissolved entirely. For the Mn-Si-rich oxide inclusions in mixed precipitates, SSTC2 resulted in the diffusion of not only Mn but also Si and O from the inclusions to the matrix. In P9₂ and P10₂, the Cr concentration increased and decreased, respectively, in their Cr-rich rings. In P2₂, a second Cr-rich ring formed. Meanwhile, in the non-oxide inclusions of P4₂, P6₂, P8₂, a redistribution of Mo-Cr-P-S, Cr-P-S and Mo-P occurred, respectively.

SSTC2 resulted in a decrease in size for P1₂, P2₂ and P11₂ and an increase in size for two inclusions in P4₂.

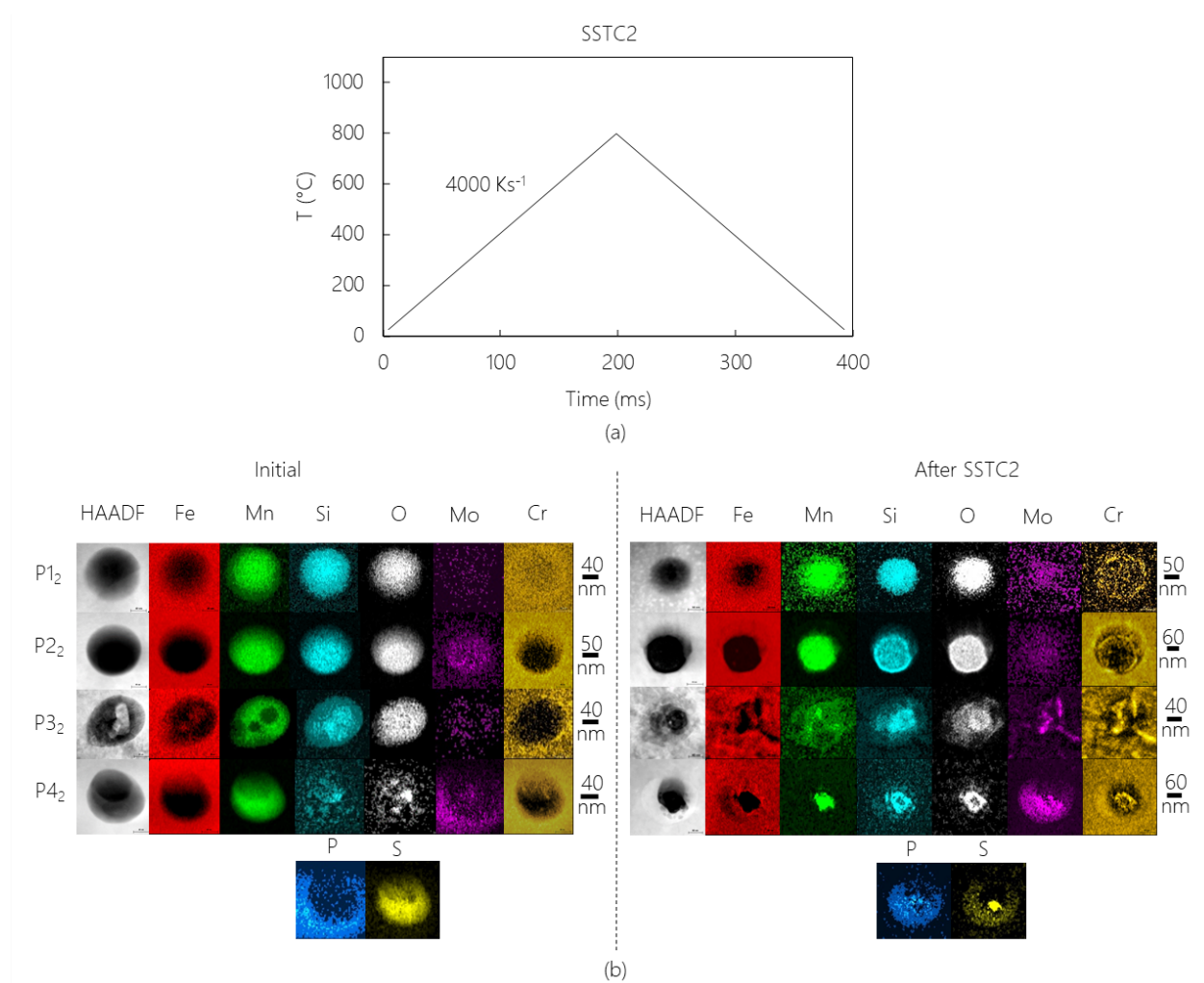


Figure 5: (a) Temperature v/s time curve for SSTC2. (b) HAADF STEM images and EDS maps of one oxide and three mixed precipitates before and after SSTC2.

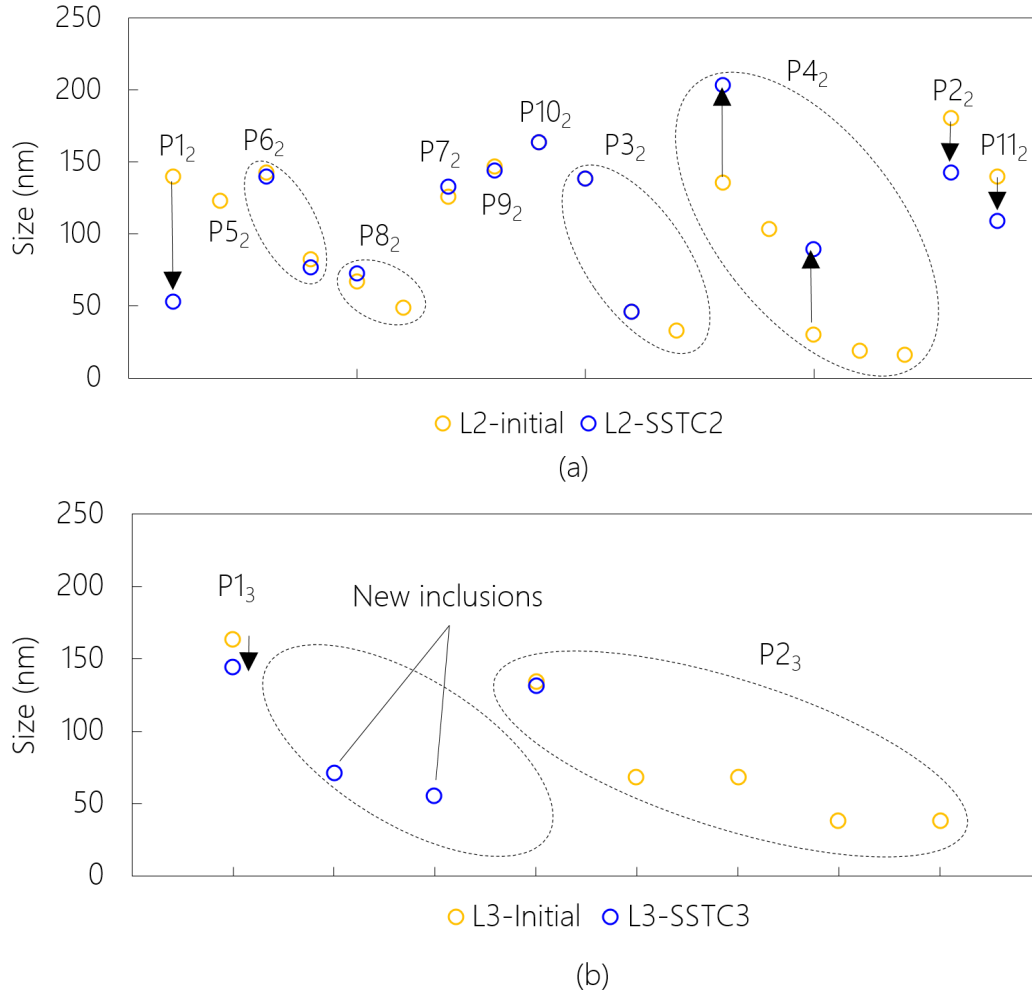


Figure 7: Precipitate size evolution in (a) L2 and (b) L3 before and after their respective SSTCs. Inclusions belonging to the same mixed precipitates are inside dashed ellipses. Arrows indicate a significant increase/decrease.

SSTC3 resulted in a decrease in size of the oxide zone in P1₃. This size decrease is due to the formation of the Fe-Mo-P-S-rich inclusion. There is no change in size of the inclusions in P2₃.

3.3 Role of the number of heating-cooling cycles and of the minimum temperature

Two lamellae, L4 and L5, were subjected to multiple heating-cooling cycles with different temperature rates and amplitudes, SSTC4 and SSTC5, respectively.

SSTC4 resembles an SSTC that could occur during an AM process without any dwell time between successive builds. The first heating cycle in SSTC4 is the same as SSTC1b i.e., heating from RT up to 1000 °C at a rate of 4000 K/s and cooling to 100 °C at the same rate. In the subsequent cycles, the maximum temperature was reduced by 50 °C and the minimum temperature was increased by 50 °C for each heating-cooling sequence until the amplitude of 600 °C was reached before the final cooling. In other words, for each cycle the total amplitude reduction was 100 °C. The temperature rates were reduced after each cycle but kept the same during a heating-cooling sequence. Fig. 8a shows the temperature v/s time curve for SSTC4.

During AM, depending on the printing speed, printing direction, or the dwell time between successive layer depositions, the sample being built may cool down to RT between each layer deposition. To reproduce this kind of SSTC, L5 was subjected to SSTC5a whose temperature v/s time curve is shown in Fig. 9a. The first cycle of SSTC5a is the same as that of SSTC1b. Then, for each successive heating-cooling sequence, the maximum temperature was decreased by 100 °C in order to have the same amplitude reduction as SSTC4, and the temperature rate was decreased by 1000 K/s, until reaching 600 °C before the final cooling down to RT.

3.3.1 Initial states of L4 and L5

In the initial state, L4 contained 8 precipitates: 5 Mn-Si-rich oxides (P3₄, P4₄, P6₄, P7₄ and P8₄) and 3 mixed (large oxide inclusion surrounded by a non-oxide ring: Mo-Cr ring for P1₄ and Cr rings for P2₄ and P5₄). Fig. 8b shows the HAADF images and EDS maps of the precipitates in L4. In the initial state, L5 contained 5 precipitates: 1 Mn-Si-rich oxide (P3₅) and 4 mixed. Amongst the mixed precipitates, 3 were oxide inclusions surrounded by non-oxide rings (Mo-Cr-rich ring for P1₅, Mo-Cr-P-rich ring for P4₅ and Cr-rich ring for P2₅), and the last one (P5₅) was a 2-zone precipitate composed of Mn-Mo-S-rich inclusion and Si-O-Cr-rich inclusion. Fig. 9b shows the HAADF images and EDS maps of the precipitates in L5. Fig. 10 shows the size evolution of the precipitates in L4 and L5.

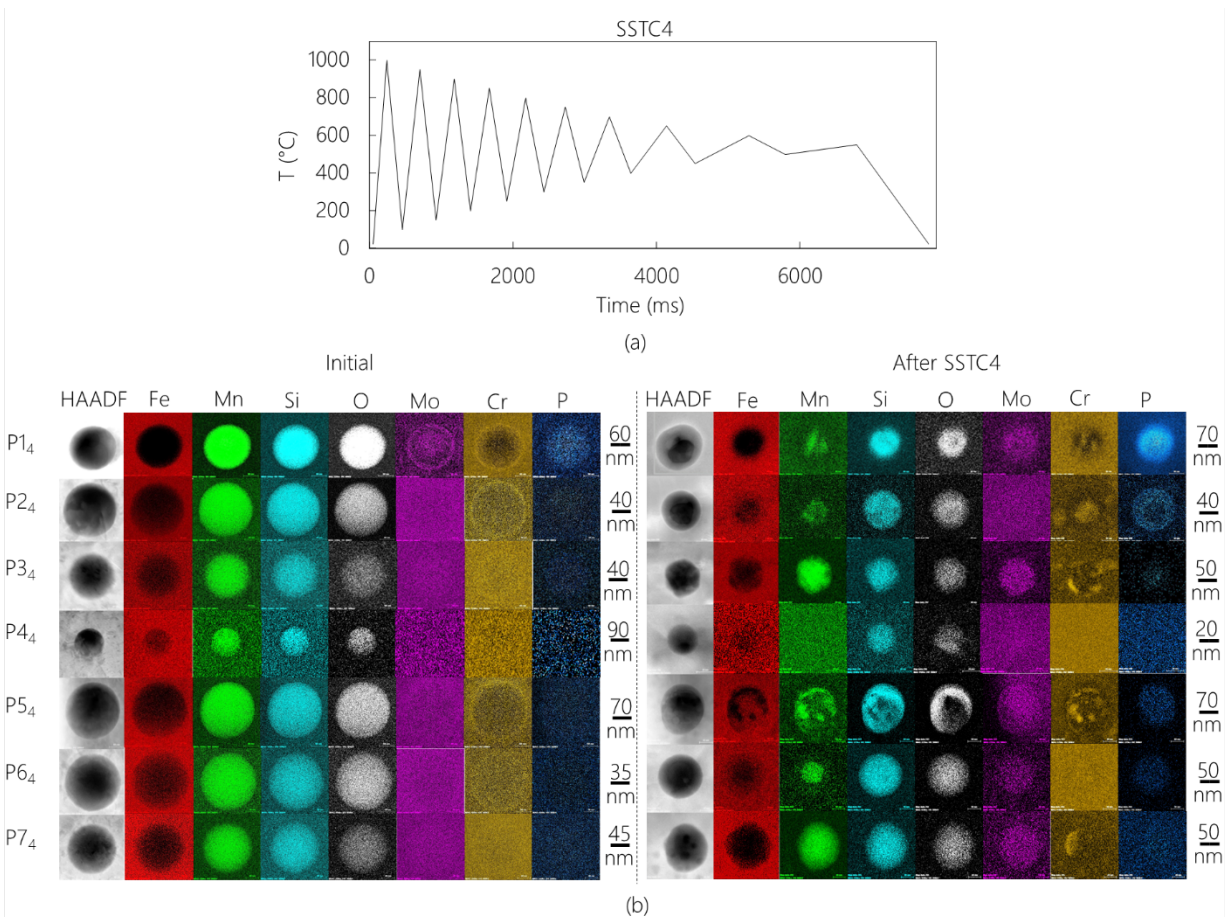


Figure 8: (a) Temperature v/s time curve of SSTC4. (b) HAADF STEM images and EDS maps of all precipitates in L4 before and after SSTC4.

3.3.2 L4 after SSTC4

After SSTC4, the oxide P8₄ completely disappeared and the remaining oxides were depleted in Mn due to its diffusion into the surrounding matrix. In addition, the Mo content in the matrix surrounding the oxides decreased but it remained unchanged in the matrix above/below these oxides. Furthermore, discontinuous Cr-rich rings formed around the oxides. Meanwhile, for all the mixed precipitates, Cr-rich rings disappeared, Mn partly diffused into the matrix, Cr redistributed, both Mn and Cr concentrated in the same regions, Mo and P content increased and Fe encroached onto precipitate boundaries. Furthermore, SSTC4 resulted in a size decrease ranging from ~10 nm to ~140 nm.

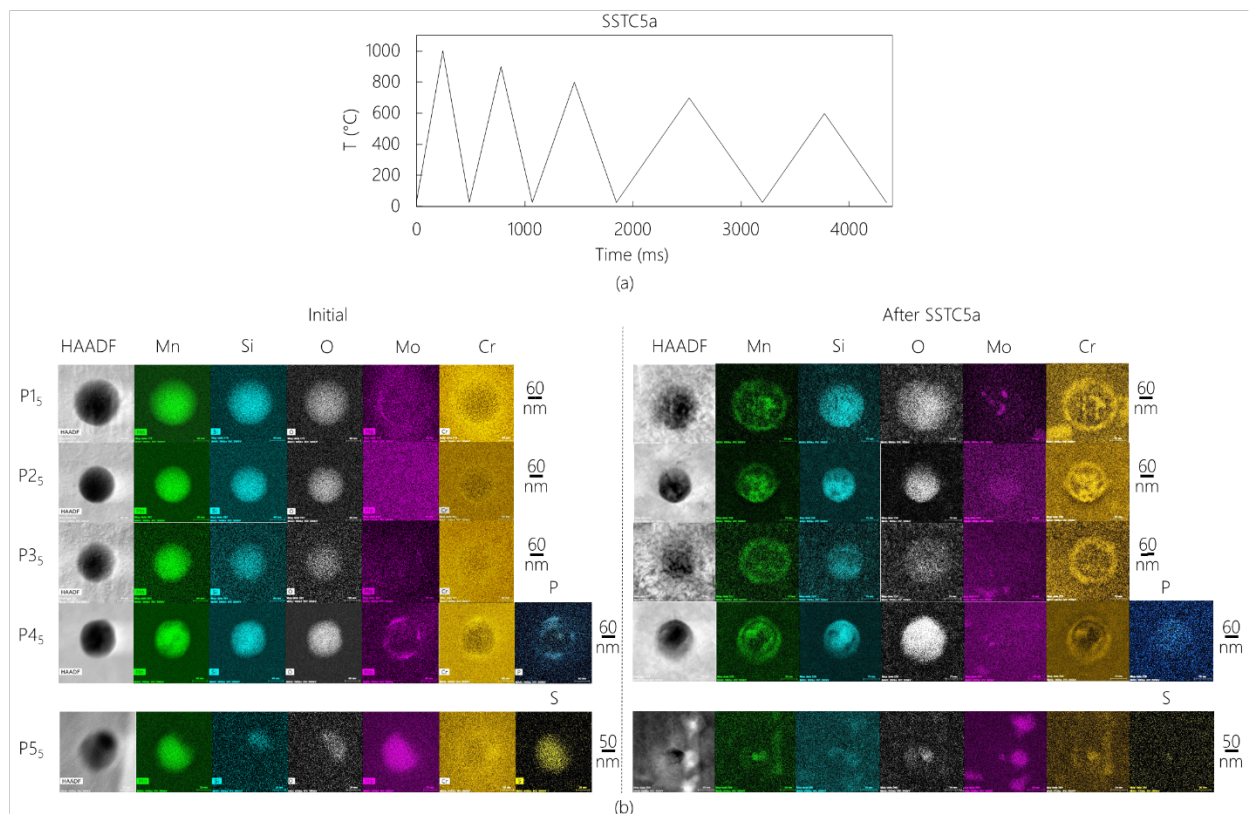


Figure 9: (a) Temperature v/s time curve of SSTC5a. (b) HAADF STEM images and EDS maps of all precipitates in L5 before (same as in [30] obtained through Creative Commons Attribution 4.0 International [CC by 4.0](https://creativecommons.org/licenses/by/4.0/) license) and after SSTC5a.

3.3.3 L5 after SSTC5a

After SSTC5a, an Mn-Cr-rich ring formed around the oxide P3₅. Furthermore, Si diffused from this oxide to the surrounding matrix and the oxide size increased. For the mixed precipitates P1₅, P2₅ and P4₅, the Cr-rich rings surrounding them were accentuated, an Mn-rich ring formed, Si diffused from the borders of the oxide zones and the oxide size increased. In addition, specifically for P2₅, an Mo-P-S-rich zone became partially superimposed on the oxide zone. For P4₅, the P-rich discontinuous ring disappeared. For P5₅, the Mn-Mo-S-rich inclusion disappeared leaving behind the Si-O-Cr-rich inclusion.

The sizes of all precipitates increased due to the formation of Mn-Cr rings along with the growth of the oxide regions.

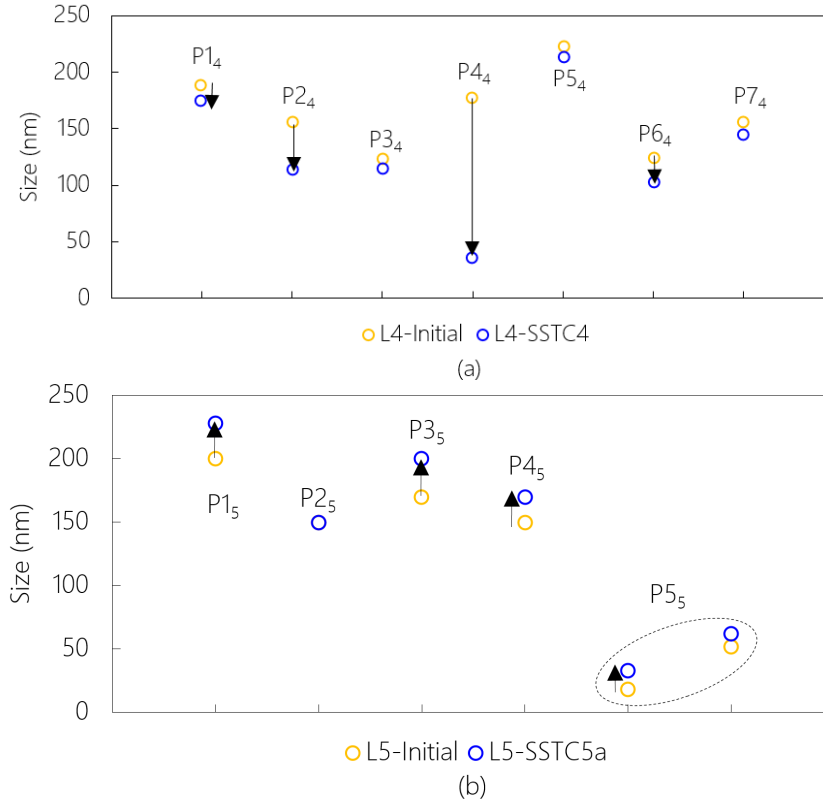


Figure 10: Precipitate size evolution for (a) L4 and (b) L5. Inclusions belonging to the same mixed precipitates are inside dashed ellipses. Arrows indicate a significant increase/decrease.

3.4. Role of annealing

Two studies were performed to understand the effect of post-process annealing on precipitate evolution. In the first study, L5, which had already experienced SSTC5a, was subjected to SSTC5b: a 1-hour annealing at 600 °C (not shown). SSTC5b did not change the size, morphology or composition of any precipitate in L5. However, it resulted in the formation of randomly distributed clusters of Mn-Cr-Mo everywhere in the matrix.

In the second study, another lamella, L6, was subjected to SSTC6: a 1-hour annealing at 700 °C. The temperature v/s time curve for SSTC6 is shown in Fig. 11a. In the initial state, L6 contained 5 precipitates, which were all oxides. After SSTC6, all precipitates experienced an enrichment in Cr, Mo, Si and O (Fig. 11b). Similar to SSTC5b, SSTC6 resulted in the formation of clusters everywhere in the lamella, however these clusters were only rich in Cr as shown in Fig. 12. Fig. 13 shows the evolution of precipitate sizes in L6. In general, SSTC6 resulted in a decrease in the size of all the precipitates. In addition, the morphology of these precipitates changed from spherical to irregular concave shapes.

Annealing temperatures for 316LSS are typically in the range from 1000 °C to 1100 °C. In-situ TEM annealing was also performed at 1000 °C, however, the lamella melted during the initial heating. This melting can be caused by two main reasons: (i) lowering of the melting point in vacuum ($\sim 10^{-5}$ Pa for the Titan³ TEM) and (ii) thickness of the lamellae (< 100 nm).

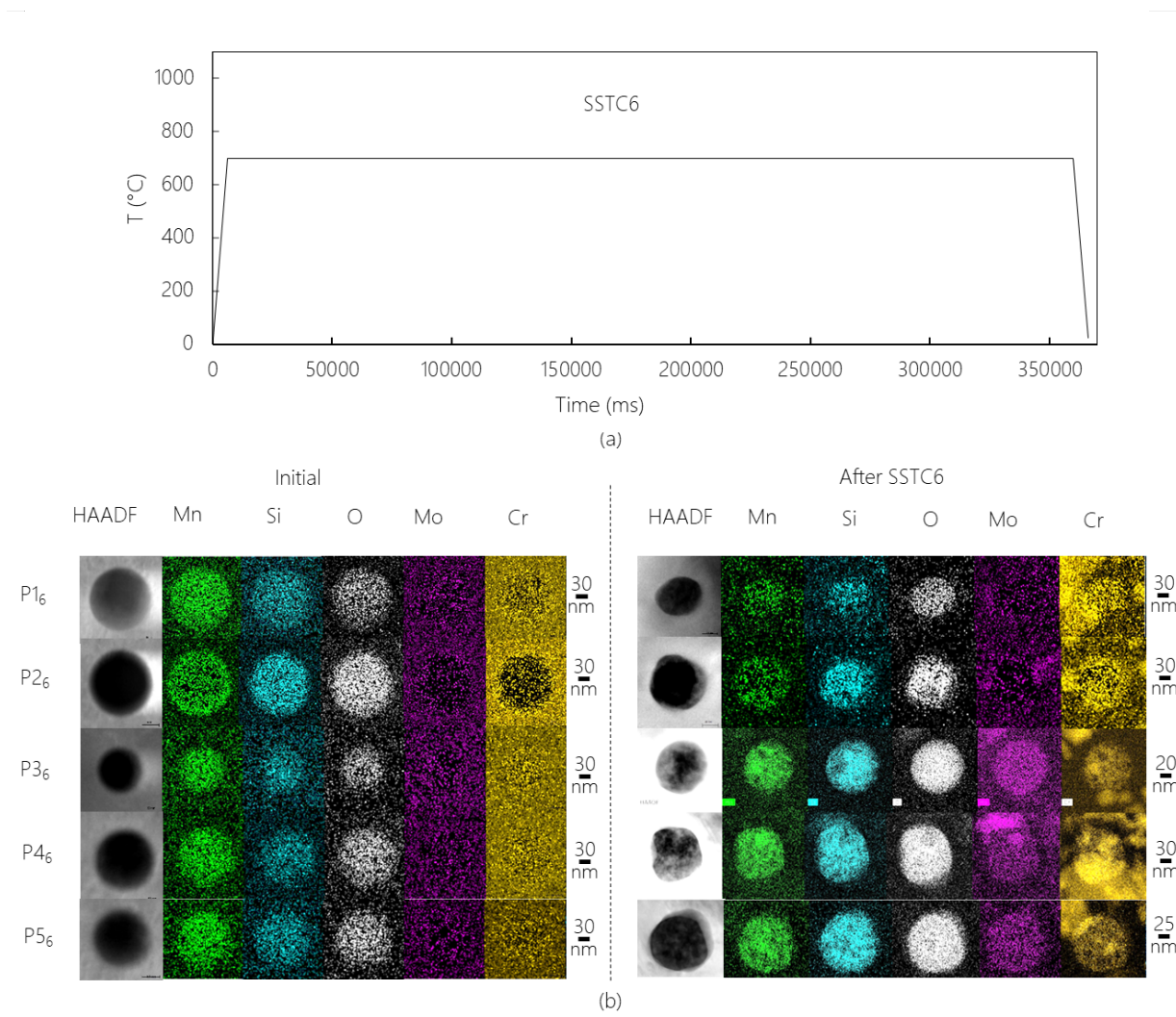


Figure 11: (a) Temperature v/s time curve of SSTC6. (b) HAADF STEM images and EDS maps of the precipitates in L6.

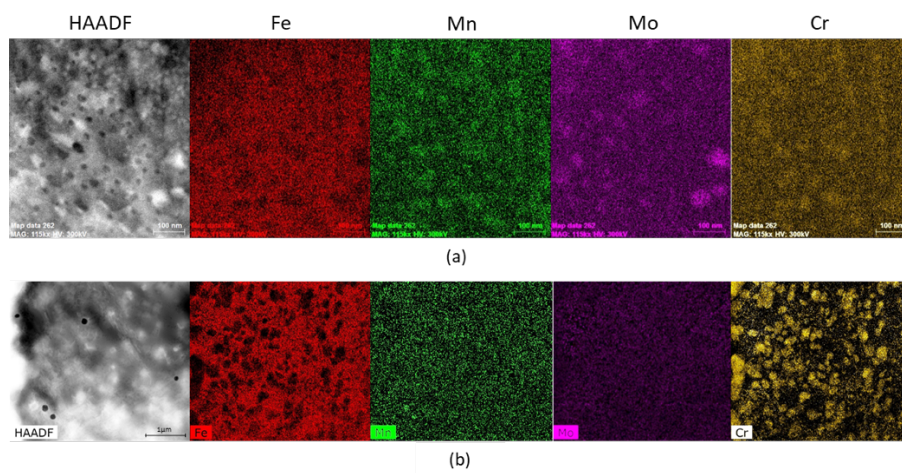


Figure 12: HAADF STEM images and EDS maps showing microsegregations (a) of Mn, Mo and Cr in L5 after SSTC5b (b) and of Cr in L6 after SSTC6 (the segregating elements are substituted with Fe atoms)

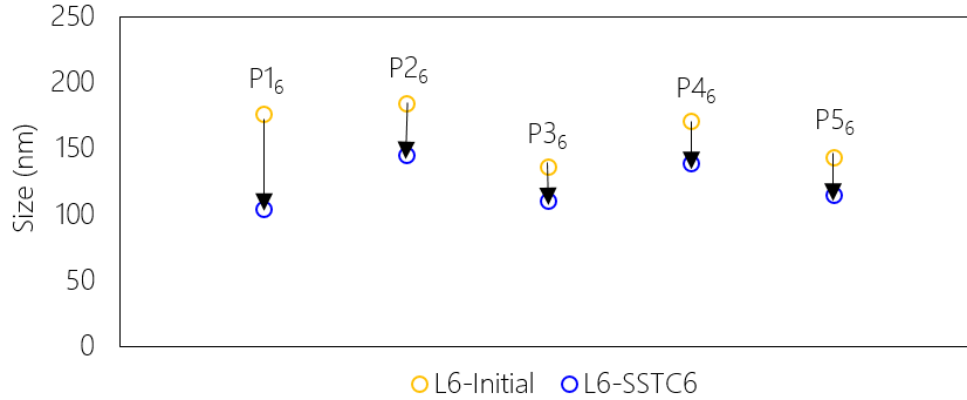


Figure 13: Evolution of the precipitate size for L5 before and after SSTC5a. Arrows indicate a significant decrease in size.

4. Discussion

The results in section 3 show that it is indeed possible for precipitates to form, disappear and evolve during SSTC. The results also show that some precipitate evolutions are common to nearly all the SSTCs studied in this work. In the following, we first discuss these general trends and their possible origins. Then, we discuss the specific role of temperature amplitude, temperature rate and the type and number of cycles, and post-process annealing on precipitate evolution.

4.1 General trends

The following common trends in SSTC-induced precipitate evolution were observed from the in-situ TEM SSTC experiments:

- Diffusion of (mainly) Mn and (some) Si from Mn-Si-rich oxide precipitates/inclusions into the surrounding austenite matrix
- Formation of Cr-rich rings around oxide precipitates/inclusions
- Shrinkage of S distribution in non-oxide precipitates/inclusions

In order to verify whether these observations are representative or not of the changes occurring due to SSTC during AM of bulk 316LSS samples, a comparison is performed with the results reported in [30]. In that work, a 60-layer wall was built using the same LMD parameters as those used in this work and two TEM lamellae, L4' and L5' (named L4 and L5, respectively, in that work), were extracted from the top and bottom layers of that wall, respectively. During the LMD process, after solidification, the material of L4' had been subjected to 59 SSTCs starting from the solidus with rapid cooling and progressively decreasing in temperature amplitude and rates in the subsequent SSTCs. Whereas, L5' had only experienced a single rapid cooling from the solidus to the room temperature. L4' had 17 precipitates out of which 2 were pure oxides and 15 were mixed. L5' had 14 precipitates out of which 2 were pure oxides and 12 were mixed precipitates.

Amongst the 27 mixed precipitates present within those two lamellae [30], 18 (~67%) were found to have clear Cr-rings around oxide inclusions and 4 others had Cr-concentrations at the locations of oxides. While the origin of these Cr-rich rings was not clear in that work, the observations of the present work clearly show for the first time that this phenomenon can be a

direct consequence of rapid cooling in the solid-state or multi-cycle SSTC. Furthermore, some precipitates studied in this work show fragmented lumps of Cr after single-cycle and multi-cycle SSTCs. Such fragmentations are also observed in the precipitates in the 60-layer wall studied in [30]. This is an important argument in favor of at least some representativeness of the results of this study and the precipitate evolutions occurring due to SSTC during AM of bulk samples. Similar arguments can be used for S concentrations that are observed in some precipitates in this work and in [30]. However, similar conclusions are hard to draw for Mn diffusion into the matrix, but its repeated occurrence strongly suggests that this could occur due to SSTC during AM. In the following, we investigate the possible origin of these observations.

The diffusion coefficients and the phase stability of different $Mn_xSi_yO_z$ oxides play an important role in determining the diffusion of (mainly) Mn and (some) Si from the Mn-Si-rich oxide precipitates/inclusions to the surrounding matrix. According to Fig. S1, Si has a higher diffusion coefficient in austenite than Mn at all the temperatures studied. However, the diffusion coefficient of Mn is higher in MnO than that of Si [36]; data on diffusion coefficients of Mn and Si in other Mn-Si-rich oxides is not known. Meanwhile, according to the Ellingham diagram [37], SiO_2 is the most stable compound amongst all the possible $Mn_xSi_yO_z$ ($x, y \geq 0, z > 0$) compounds i.e., the formation of this compound results in the highest decrease in Gibbs free energy. The higher stability of the SiO_2 phase in comparison to other $Mn_xSi_yO_z$ phases and higher diffusivity of Mn in MnO suggests that it would be easier for Mn atoms to diffuse away from the precipitate than Si atoms. This understanding is applicable to both thin-film and bulk materials.

The Cr-rich rings and zones forming respectively around and inside the oxides are due to the diffusion of Cr from the matrix towards the oxides. Shibata et al. [38,39] had investigated the chemical composition changes of oxide inclusions in Mn-Si deoxidized stainless Fe-Cr-steels following a 2-hour heat treatment at 1200 °C. For a steel with a low Si-concentration (0.2 wt. %), they evidenced a Cr-enrichment of the interface between the austenite and the MnO- SiO_2 phase [39]. For a steel with higher Si-concentration (0.84 wt. %), they observed Cr-enrichment inside the oxide. In both cases, they reported that Cr diffused from the matrix towards the oxide; furthermore, they reported that this diffusion resulted in the transformation of SiO_2 and MnO- SiO_2 into MnO- Cr_2O_3 . In the present study, where the Si concentration in the 316LSS is 0.7 wt. %, Cr-rich rings are formed around oxides in the majority of cases. In some cases, however, existing Cr-rich rings have disappeared and Cr-rich zones (bands, circular and crescent-shaped clusters) appeared inside the precipitates. The data from the EDS line profile analysis shows that in these cases, the Cr concentration increases inside these precipitates and not in their surrounding matrix, which suggests that a diffusion of Cr took place from the prior rings towards the center of the precipitates. The observations of the present study suggest a trend that is similar to the trend reported in the study of Shibata et al. [38,39] i.e., the diffusion of Cr either from the matrix to the precipitate interface or from the precipitate interface to the precipitate core.

S has the highest diffusion coefficient in austenite amongst all the substitutional elements present in 316LSS (Fig. S1). While the diffusion coefficient of S is not known inside the non-oxide precipitates, the observations that show shrinkage of S into smaller zones within non-oxide precipitates suggests that S should also have a high diffusion coefficient inside them.

Note that the above discussion on diffusion coefficients and phase stability provides a preliminary understanding of the origin of the aforementioned observations. Along with these, other factors that should contribute to precipitate evolution are: (a) Variations in proportion of elements between precipitates resulting in formation of different compounds for similar kind of precipitates e.g., Mn-Si-rich oxides could have different $Mn_xSi_yO_z$ ($x, y \geq 0, z > 0$) compositions. (b) Different crystallographic orientation of each lamella, unique neighborhoods of each

precipitate, 2D surface effects, and the nature of the applied SSTC all contribute to the local thermodynamic driving forces that determine the evolution of each precipitate. (c) A plane stress state is generated in the lamellae during SSTC due to thermal stresses induced by the differences in the thermal moduli of the lamellae, the electrothermal chips and the tungsten deposition via FIB to attach the lamellae to the chips. While it is difficult to quantify the impact of each of these factors on precipitate evolution, nevertheless, their contribution together with the diffusion coefficients and phase stabilities of different compounds must determine the observed differences in the evolution of precipitates of the same kind. Precipitation kinetics simulations can be used to take into account these additional factors and the results of this work can serve as validation for such simulations.

4.2 Role of temperature amplitude

The results from section 3.1 clearly show that for the same temperature rate, SSTCs with higher temperature amplitudes result in significantly more changes to precipitates than SSTCs at lower temperature amplitudes. A higher temperature amplitude while keeping the temperature rate constant provides stronger chemo-thermo-mechanical driving forces and a longer time for diffusion.

Another approach to compare the role of temperature amplitude could have been to keep the duration of the SSTC constant instead of the temperature rate; for example, SSTC1a (heating from RT to 500 °C and cooling down to RT at 4000 K/s) could have been performed at 1948.7 K/s so that instead of 0.11875 s, the duration of this SSTC would have been 0.24375 s, which is the same duration as that of SSTC1b. Since precipitate evolution is a mass transfer process, a longer time for the same temperature amplitude should result in more changes. The disadvantage of this approach is that both temperature amplitude and temperature rate are different, which makes it difficult to separate their role on the precipitate evolution.

4.3 Role of temperature rate

As discussed at the end of section 4.2, a longer time for the same temperature amplitude should result in more changes. The experiment at lower temperature rate (1000 K/s v/s 4000 K/s) with the same maximum temperature (800 °C) resulted in the formation of Fe-Mo-P-S-rich inclusions on an oxide that was already present in the material. This suggests that the matrix started encroaching on the oxide boundaries, and that the oxide would have dissolved entirely if a slower temperature were to be applied. Kim et al. [40] performed cooling experiments at different temperature rates ($< 10^1$ K/s) to study the evolution of Mn-Si-rich oxide precipitates in an Mn/Si deoxidized steel. They reported the growth of two Mn-S precipitates on Mn-Si-rich oxides with a shape and profile that is very similar to the profile of the two Fe-Mo-P-S-rich inclusions that grew into the oxide of P1₃ in Fig. 6. While it is not appropriate to perform a one-to-one correlation between the present study and the study of Kim et al. [40], the similarity between the two results suggests that the growth of new precipitates or the dissolution of existing precipitates observed in the present work is indeed possible in bulk materials.

4.4 Role of the number and type of SSTC

SSTC4 and SSTC5a were multiple cycles with cooling down to $T > RT$ and $T = RT$, respectively, after each heating-cooling sequence. In general, they resulted in more changes than

the SSTCs with only one cycle. In addition to (i) Mn, Si and O diffusion, (ii) shrinkage in S distribution and (iii) morphology change for some precipitates, two common trends for the multiple cycles were observed: an enrichment in P for mixed precipitates and a migration of Mn and Cr to the exact same regions.

Between SSTC4 and SSTC5a, the main difference was with respect to the evolution of the Cr-rich rings surrounding oxide precipitates. SSTC4 resulted in the disappearance of Cr-rich rings; the Cr atoms migrated from the precipitate interface to form high-concentration regions inside the precipitates. Whereas SSTC5a resulted in the accentuation of the already existing Cr-rich rings, which also became rich in Mn.

The formation of Mn-Cr-rich rings can be explained by their respective diffusion coefficients in austenite and in the precipitates. According to Fig. S1, the diffusion coefficient of Cr in austenite is higher than that of Mn. Furthermore, as mentioned in section 4.1, the diffusion coefficient of Mn is higher in MnO inclusions than in the austenite metal matrix [36]. It is clear that Mn tends to diffuse away from the oxide inclusion and towards the matrix, however, the presence of the Cr-rich rings between the oxide and the matrix, and the influx of Cr into these rings, may act as a barrier to the transport of Mn from the oxide to the matrix, resulting in the Mn enrichment of these rings. Note that the previous statement is merely a hypothesis, which is difficult to confirm because it requires performing operando experiments to track the migration of different Mn and Cr atoms.

Note that if one were given lamellae L1 and L4(or L5) in their final states i.e., after being subjected to SSTC1b and SSTC4(or SSTC5a), respectively, then one would find it difficult to identify which lamella has been subjected to what SSTC. This is because in their final states, these lamellae do not exhibit dramatic differences in their precipitate size or composition. This result is consistent with the precipitates observed in lamellae L4' and L5' (see definition in section 4.1) extracted from the bottom and top layers, respectively, of the 60-layer wall studied in [30]. It is thanks to the in-situ TEM SSTC experiments performed in this work that one can deduce that multiple SSTCs could indeed induce more changes to the precipitate structure than those occurring during 1-cycle high-amplitude rapid SSTC.

4.5 Role of annealing

Annealing for 1 hour at 700 °C resulted in an enrichment in Mo, Cr, Si and O of the oxides. Similar observations have been reported by Chao et al. [41] on an SLM 316LSS after a 2-hour annealing at 800 °C. A reduction in precipitate size was also observed, which implies that the elements in the precipitates diffuse into the matrix; a phenomenon that is expected to occur during annealing. However, annealing for 1 hour at both 600 °C and 700 °C also resulted in the disappearance of the Mo-Cr-rich (also Mn-rich for L5) cellular solidification structures and led to the formation of randomly distributed clusters of Mn-Cr-Mo everywhere in the lamellae L5 and L6. Such clusters have never been reported in other studies and it is very likely that they are artefacts of the very small thickness of the TEM lamellae and the long duration at elevated temperatures under high vacuum, which can result in, for example, desorption of some of the elements; in contrast, the rapid SSTCs studied in this work occur in time spans that are several orders of magnitude lower than those occurring during annealing and the elements have negligibly smaller time span to desorb. This result suggests that the aforementioned observations from in-situ TEM annealing experiments may not be representative of the precipitate evolutions occurring during annealing of bulk materials.

5. Conclusions

The main aim of this work was to understand the role of different factors of SSTC (Solid-State Thermal Cycling) such as temperature amplitude and rates, the number and type of SSTC, and post-process annealing on the evolution of precipitates during LMD (Laser Metal Deposition) of a 316LSS. In order to do this, we first prepared LMD 316LSS samples, extracted TEM lamellae, subjected these lamellae to SSTC inside a transmission electron microscope and studied the precipitate evolution before and after SSTC via HAADF imaging and EDS mapping. This in-situ TEM SSTC study helped identify the role of different factors of SSTC on the evolution of the composition, size and morphology of submicron-sized precipitates in LMD 316LSS. Below are the conclusions of these experiments.

- The changes that occurred after all SSTCs studied in this work were: (1) diffusion of (mainly) Mn and (some) Si from Mn-Si-rich oxide precipitates/inclusions into surrounding matrix, (2) formation of Cr-rich rings around oxide precipitates/inclusions and (3) shrinkage of S distribution in non-oxide precipitates/inclusions. Cr-rings surrounding oxide inclusions and local concentrations of S in non-oxide precipitates/inclusions were also reported in precipitates in bulk LMD 316LSS samples studied in [30], which strongly suggests that the aforementioned changes could also occur due to SSTC during AM of bulk 316LSS. In particular, major changes to precipitate structure and composition should occur in the initial stages of SSTC (during the first or few cycles after solidification). The later stages of SSTC could enhance these phenomena or bring about additional changes; however, the nature and type of these changes will depend on the nature and duration of the SSTC.
- For the same temperature rate, a higher temperature amplitude results in significantly more changes to precipitate structure and composition. Since precipitate evolution is a mass transfer process, a higher temperature amplitude at the same temperature allows more time for changes to occur. Furthermore, a higher temperature amplitude provides stronger chemo-thermo-mechanical driving forces.
- For the same temperature amplitude, a lower temperature rate results in more changes to the precipitate structure and composition. Specifically, for the lower temperature rate studied in this work, the nucleation and growth of two Fe-Mo-P-S-rich inclusions at the expense of an existing oxide inclusion was observed.
- Multi-cycle SSTCs in general result in more changes to precipitate structure and composition than single-cycle SSTCs. Along with the changes observed during single-cycle SSTCs, multi-cycle SSTCs induced an enrichment in P for mixed precipitates and a migration of both Cr and Mn in the same regions. In addition, depending on the type of the multi-cycle SSTC, other changes that can occur are: (i) disappearance of Cr-rich rings, (ii) formation of high-concentration regions of Cr inside precipitates and (iii) total dissolution of an oxide, (iv) formation of Mn-Cr-rings and Mn-Cr-rich regions respectively around and inside most precipitates.
- Annealing for 1 hour at 600 °C and at 700 °C resulted in the disappearance of the Mo-Cr-rich cellular solidification structures and led to the formation of randomly distributed clusters in the lamellae. These clusters are likely to be artefacts of the very small thickness of the TEM lamellae and elevated temperatures for a very long duration (several orders of magnitude higher than the other SSTCs studied in this work) under high vacuum, which can cause, for example, desorption of some of the elements.

- Precipitate sizes were also measured after each SSTC, in general, however, no conclusive evidence indicating a general increase or decrease in the precipitate size could be obtained. This could be a consequence of the fact that precipitate growth/shrinkage involves transport of atoms in the bulk material, which is a time-consuming process, and the time span during which the lamellae were subjected to SSTC may not be sufficient to observe precipitate size changes. Whether or not the SSTC occurring during AM of large samples results in significant changes to precipitate sizes, still remains an open question.

The results of this study for the first time open a viewport into understanding the evolution of submicron-sized precipitates during AM of 316LSS. This understanding can be transformed into developing and validating precipitation kinetics models that can be used to gain a deep understanding of the non-equilibrium evolution of precipitates in bulk samples. Furthermore, the proposed technique of in-situ TEM SSTC experiments can be applied to study precipitate evolution in any material system that exhibits submicron-sized precipitates. It can also be used to study SSTC-driven interactions between dislocations and precipitates in order to better understand how dislocation structures form at the location of chemical heterogeneities in additively manufactured materials.

Acknowledgments

M.B.H.S., E.H. and M.V.U. are grateful to the Fédération Francilienne de Mécanique (F2M) for their support through the Coup de Pouce 2019 grant. M.V.U. is grateful to the European Research Council (ERC) for their support through the European Union's Horizon 2020 research and innovation programme for project GAMMA (Grant agreement No. 946959). FIB-SEM and TEM work was carried out using the facilities available at the MSSMat laboratory within the MATMECA consortium, which is supported by the Agence National de la Recherche (ANR) under the contract number ANR-10-EQPX-37. Finally, the authors would like to thank Steve Gaudet (LMS, Ecole Polytechnique) for the fruitful discussions.

References

- [1] R. Sampson, R. Lancaster, M. Sutcliffe, D. Carswell, C. Hauser, J. Barras, The influence of key process parameters on melt pool geometry in direct energy deposition additive manufacturing systems, *Optics & Laser Technology*. 134 (2021) 106609. <https://doi.org/10.1016/j.optlastec.2020.106609>.
- [2] M. Cheng, X. Xiao, G. Luo, L. Song, Integrated control of molten pool morphology and solidification texture by adjusting pulse duration in laser additive manufacturing of Inconel 718, *Optics & Laser Technology*. 142 (2021) 107137. <https://doi.org/10.1016/j.optlastec.2021.107137>.
- [3] A. Chouhan, A. Aggarwal, A. Kumar, Role of melt flow dynamics on track surface morphology in the L-PBF additive manufacturing process, *International Journal of Heat and Mass Transfer*. 178 (2021) 121602. <https://doi.org/10.1016/j.ijheatmasstransfer.2021.121602>.
- [4] D. Guo, K. Yan, M.D. Callaghan, D. Daisenberger, M. Chatterton, J. Chen, A. Wisbey, W. Mirihanage, Solidification microstructure and residual stress correlations in direct energy deposited type 316L stainless steel, *Materials & Design*. 207 (2021) 109782. <https://doi.org/10.1016/j.matdes.2021.109782>.

- [5] F.L. Vecchiato, H. de Winton, P.A. Hooper, M.R. Wenman, Melt pool microstructure and morphology from single exposures in laser powder bed fusion of 316L stainless steel, *Additive Manufacturing*. 36 (2020) 101401. <https://doi.org/10.1016/j.addma.2020.101401>.
- [6] C. Kenel, D. Grolimund, X. Li, E. Panepucci, V.A. Samson, D.F. Sanchez, F. Marone, C. Leinenbach, In situ investigation of phase transformations in Ti-6Al-4V under additive manufacturing conditions combining laser melting and high-speed micro-X-ray diffraction, *Sci Rep*. 7 (2017) 1–10. <https://doi.org/10.1038/s41598-017-16760-0>.
- [7] C. Zhao, K. Fezzaa, R.W. Cunningham, H. Wen, F.D. Carlo, L. Chen, A.D. Rollett, T. Sun, Real-time monitoring of laser powder bed fusion process using high-speed X-ray imaging and diffraction, *Sci Rep*. 7 (2017) 1–11. <https://doi.org/10.1038/s41598-017-03761-2>.
- [8] C.L.A. Leung, S. Marussi, R.C. Atwood, M. Towrie, P.J. Withers, P.D. Lee, In situ X-ray imaging of defect and molten pool dynamics in laser additive manufacturing, *Nat Commun*. 9 (2018) 1–9. <https://doi.org/10.1038/s41467-018-03734-7>.
- [9] N.P. Calta, J. Wang, A.M. Kiss, A.A. Martin, P.J. Depond, G.M. Guss, V. Thampy, A.Y. Fong, J.N. Weker, K.H. Stone, C.J. Tassone, M.J. Kramer, M.F. Toney, A. Van Buuren, M.J. Matthews, An instrument for in situ time-resolved X-ray imaging and diffraction of laser powder bed fusion additive manufacturing processes, *Review of Scientific Instruments*. 89 (2018) 055101. <https://doi.org/10.1063/1.5017236>.
- [10] C. Kenel, D. Grolimund, J.L. Fife, V.A. Samson, S. Van Petegem, H. Van Swygenhoven, C. Leinenbach, Combined in situ synchrotron micro X-ray diffraction and high-speed imaging on rapidly heated and solidified Ti-48Al under additive manufacturing conditions, *Scripta Materialia*. 114 (2016) 117–120. <https://doi.org/10.1016/j.scriptamat.2015.12.009>.
- [11] S. Hocine, H. Van Swygenhoven, S. Van Petegem, C.S.T. Chang, T. Maimaitiyili, G. Tinti, D. Ferreira Sanchez, D. Grolimund, N. Casati, Operando X-ray diffraction during laser 3D printing, *Materials Today*. 34 (2020) 30–40. <https://doi.org/10.1016/j.mattod.2019.10.001>.
- [12] C. Meier, S.L. Fuchs, A.J. Hart, W.A. Wall, A novel smoothed particle hydrodynamics formulation for thermo-capillary phase change problems with focus on metal additive manufacturing melt pool modeling, *Computer Methods in Applied Mechanics and Engineering*. 381 (2021) 113812. <https://doi.org/10.1016/j.cma.2021.113812>.
- [13] T. Pinomaa, M. Lindroos, M. Walbrühl, N. Provatas, A. Laukkanen, The significance of spatial length scales and solute segregation in strengthening rapid solidification microstructures of 316L stainless steel, *Acta Materialia*. 184 (2020) 1–16. <https://doi.org/10.1016/j.actamat.2019.10.044>.
- [14] Q. Chen, L.M.D.S. Sancho, G. Guillemot, C.-A. Gandin, M. Bellet, J.-D. Bartout, M.-H. Berger, C. Colin, Level-set modelling of Laser Beam Melting process applied onto ceramic materials – Comparison with experimental results, *IOP Conf. Ser.: Mater. Sci. Eng.* 529 (2019) 012002. <https://doi.org/10.1088/1757-899X/529/1/012002>.
- [15] D. Tourret, H. Liu, J. LLorca, Phase-field modeling of microstructure evolution: Recent applications, perspectives and challenges, *ArXiv:2104.09915 [Cond-Mat]*. (2021). <http://arxiv.org/abs/2104.09915> (accessed August 17, 2021).
- [16] S. Kavousi, B.R. Novak, D. Moldovan, M. Asle Zaeem, Quantitative prediction of rapid solidification by integrated atomistic and phase-field modeling, *Acta Materialia*. 211 (2021) 116885. <https://doi.org/10.1016/j.actamat.2021.116885>.
- [17] M.M. Francois, A. Sun, W.E. King, N.J. Henson, D. Tourret, C.A. Bronkhorst, N.N. Carlson, C.K. Newman, T. Haut, J. Bakosi, J.W. Gibbs, V. Livescu, S.A. Vander Wiel, A.J. Clarke, M.W. Schraad, T. Blacker, H. Lim, T. Rodgers, S. Owen, F. Abdeljawad, J. Madison, A.T. Anderson, J.-L. Fattebert, R.M. Ferencz, N.E. Hodge, S.A. Khairallah, O. Walton, Modeling

- of additive manufacturing processes for metals: Challenges and opportunities, *Current Opinion in Solid State and Materials Science*. 21 (2017) 198–206. <https://doi.org/10.1016/j.cossms.2016.12.001>.
- [18] W. Hofmeister, M. Griffith, Solidification in direct metal deposition by LENS processing, *JOM*. 53 (2001) 30–34. <https://doi.org/10.1007/s11837-001-0066-z>.
- [19] U. Scipioni Bertoli, G. Guss, S. Wu, M.J. Matthews, J.M. Schoenung, In-situ characterization of laser-powder interaction and cooling rates through high-speed imaging of powder bed fusion additive manufacturing, *Materials & Design*. 135 (2017) 385–396. <https://doi.org/10.1016/j.matdes.2017.09.044>.
- [20] J. Yang, H. Yu, J. Yin, M. Gao, Z. Wang, X. Zeng, Formation and control of martensite in Ti-6Al-4V alloy produced by selective laser melting, *Materials & Design*. 108 (2016) 308–318. <https://doi.org/10.1016/j.matdes.2016.06.117>.
- [21] A.J. Birnbaum, J.C. Steuben, E.J. Barrick, A.P. Iliopoulos, J.G. Michopoulos, Intrinsic strain aging, Σ boundaries, and origins of cellular substructure in additively manufactured 316L, *Additive Manufacturing*. 29 (2019) 100784. <https://doi.org/10.1016/j.addma.2019.100784>.
- [22] T.R. Smith, J.D. Sugar, C. San Marchi, J.M. Schoenung, Strengthening mechanisms in directed energy deposited austenitic stainless steel, *Acta Materialia*. 164 (2019) 728–740. <https://doi.org/10.1016/j.actamat.2018.11.021>.
- [23] T.Q. Phan, M. Strantza, M.R. Hill, T.H. Gnaupel-Herold, J. Heigel, C.R. D’Elia, A.T. DeWald, B. Clausen, D.C. Pagan, J.Y. Peter Ko, D.W. Brown, L.E. Levine, Elastic Residual Strain and Stress Measurements and Corresponding Part Deflections of 3D Additive Manufacturing Builds of IN625 AM-Bench Artifacts Using Neutron Diffraction, Synchrotron X-Ray Diffraction, and Contour Method, *Integr Mater Manuf Innov*. 8 (2019) 318–334. <https://doi.org/10.1007/s40192-019-00149-0>.
- [24] K. Saeidi, L. Kvetková, F. Lofaj, Z. Shen, Austenitic stainless steel strengthened by the in situ formation of oxide nanoinclusions, *RSC Adv*. 5 (2015) 20747–20750. <https://doi.org/10.1039/C4RA16721J>.
- [25] Y.M. Wang, T. Voisin, J.T. McKeown, J. Ye, N.P. Calta, Z. Li, Z. Zeng, Y. Zhang, W. Chen, T.T. Roehling, R.T. Ott, M.K. Santala, P.J. Depond, M.J. Matthews, A.V. Hamza, T. Zhu, Additively manufactured hierarchical stainless steels with high strength and ductility, *Nature Mater*. 17 (2018) 63–71. <https://doi.org/10.1038/nmat5021>.
- [26] Q. Chao, V. Cruz, S. Thomas, N. Birbilis, P. Collins, A. Taylor, P.D. Hodgson, D. Fabijanic, On the enhanced corrosion resistance of a selective laser melted austenitic stainless steel, *Scripta Materialia*. 141 (2017) 94–98. <https://doi.org/10.1016/j.scriptamat.2017.07.037>.
- [27] D.-R. Eo, S.-H. Park, J.-W. Cho, Inclusion evolution in additive manufactured 316L stainless steel by laser metal deposition process, *Materials & Design*. 155 (2018) 212–219. <https://doi.org/10.1016/j.matdes.2018.06.001>.
- [28] Z.E. Tan, J.H.L. Pang, J. Kaminski, H. Pepin, Characterisation of porosity, density, and microstructure of directed energy deposited stainless steel AISI 316L, *Additive Manufacturing*. 25 (2019) 286–296. <https://doi.org/10.1016/j.addma.2018.11.014>.
- [29] P. Deng, M. Karadge, R.B. Rebak, V.K. Gupta, B.C. Prorok, X. Lou, The origin and formation of oxygen inclusions in austenitic stainless steels manufactured by laser powder bed fusion, *Additive Manufacturing*. (2020) 101334. <https://doi.org/10.1016/j.addma.2020.101334>.
- [30] M.V. Upadhyay, M.B.H. Slama, S. Gaudez, N. Mohanan, L. Yedra, S. Hallais, E. Hérigné, A. Tanguy, Non-oxide precipitates in additively manufactured austenitic stainless steel, *Sci Rep*. 11 (2021) 10393. <https://doi.org/10.1038/s41598-021-89873-2>.

- [31] J.S. Kim, T. LaGrange, B.W. Reed, M.L. Taheri, M.R. Armstrong, W.E. King, N.D. Browning, G.H. Campbell, Imaging of Transient Structures Using Nanosecond in Situ TEM, *Science*. 321 (2008) 1472–1475. <https://doi.org/10.1126/science.1161517>.
- [32] A. Kulovits, J.M.K. Wiezorek, T. LaGrange, B.W. Reed, G.H. Campbell, Revealing the transient states of rapid solidification in aluminum thin films using ultrafast in situ transmission electron microscopy, *Philosophical Magazine Letters*. 91 (2011) 287–296. <https://doi.org/10.1080/09500839.2011.558030>.
- [33] Höganäs portfolio for additive manufacturing (https://www.hoganas.com/globalassets/download-media/sharepoint/brochures-and-datasheets---all-documents/additive-manufacturing_hoganas-additive-standard-portfolio_2853hog.pdf), (n.d.). https://www.hoganas.com/globalassets/download-media/sharepoint/brochures-and-datasheets---all-documents/additive-manufacturing_hoganas-additive-standard-portfolio_2853hog.pdf.
- [34] K.M. Bertsch, G. Meric de Bellefon, B. Kuehl, D.J. Thoma, Origin of dislocation structures in an additively manufactured austenitic stainless steel 316L, *Acta Materialia*. 199 (2020) 19–33. <https://doi.org/10.1016/j.actamat.2020.07.063>.
- [35] T. DebRoy, H.L. Wei, J.S. Zuback, T. Mukherjee, J.W. Elmer, J.O. Milewski, A.M. Beese, A. Wilson-Heid, A. De, W. Zhang, Additive manufacturing of metallic components – Process, structure and properties, *Progress in Materials Science*. 92 (2018) 112–224. <https://doi.org/10.1016/j.pmatsci.2017.10.001>.
- [36] J. Dudała, J. Gilewicz-Wolter, Z. Stęgowski, Simultaneous measurement of Cr, Mn and Fe diffusion in chromium-manganese steels, *Nukleonika*. Vol. 50 (2005) 67–71.
- [37] H.J.T. Ellingham, Reducibility of oxides and sulphides in metallurgical processes, *Journal of the Society of Chemical Industry*. 63 (1944) 125–160. <https://doi.org/10.1002/jctb.5000630501>.
- [38] H. Shibata, T. Tanaka, K. Kimura, S.-Y. Kitamura, Composition change in oxide inclusions of stainless steel by heat treatment, *Ironmaking & Steelmaking*. 37 (2010) 522–528. <https://doi.org/10.1179/030192310X12700328925903>.
- [39] H. Shibata, K. Kimura, T. Tanaka, S. Kitamura, Mechanism of Change in Chemical Composition of Oxide Inclusions in Fe–Cr Alloys Deoxidized with Mn and Si by Heat Treatment at 1473 K, *ISIJ Int*. 51 (2011) 1944–1950. <https://doi.org/10.2355/isijinternational.51.1944>.
- [40] H.S. Kim, H.-G. Lee, K.-S. Oh, MnS precipitation in association with manganese silicate inclusions in Si/Mn deoxidized steel, *Metall Mater Trans A*. 32 (2001) 1519. <https://doi.org/10.1007/s11661-001-0239-y>.
- [41] Q. Chao, S. Thomas, N. Birbilis, P. Cizek, P.D. Hodgson, D. Fabijanic, The effect of post-processing heat treatment on the microstructure, residual stress and mechanical properties of selective laser melted 316L stainless steel, *Materials Science and Engineering: A*. 821 (2021) 141611. <https://doi.org/10.1016/j.msea.2021.141611>.